Powerful ordered collective heat engines

Fernando S. Filho [1], Gustavo A. L. Forão [1], Daniel M. Busiello [2,*], B. Cleuren [3] and Carlos E. Fiore [1]

[1] *Universidade de São Paulo, Instituto de Física, Rua do Matão, 1371, 05508-090 São Paulo, SP, Brazil*

[2] *Max Planck Institute for the Physics of Complex Systems, 01187 Dresden, Germany*

[3] *UHasselt, Faculty of Sciences, Theory Lab, Agoralaan, 3590 Diepenbeek, Belgium*

(Received 6 February 2023; accepted 26 September 2023; published 20 October 2023)

We introduce a class of stochastic engines in which the regime of units operating synchronously can boost the performance. Our approach encompasses a minimal setup composed of N interacting units placed in contact with two thermal baths and subjected to a constant driving worksource. The interplay between unit synchronization and interaction leads to an efficiency at maximum power between the Carnot η_c and the Curzon-Ahlborn bound η_{CA}. Moreover, these limits can be respectively saturated maximizing the efficiency, and by simultaneous optimization of power and efficiency. We show that the interplay between Ising-like interactions and a collective ordered regime is crucial to operate as a heat engine. The main system features are investigated by means of a linear analysis near equilibrium, and developing an effective discrete-state model that captures the effects of the synchronous phase. The robustness of our findings extends beyond the all-to-all interactions and paves the way for the building of promising nonequilibrium thermal machines based on ordered structures.

DOI: 10.1103/PhysRevResearch.5.043067

I. INTRODUCTION

The ambition to build efficient engines is not only prominent, but also pressing in thermodynamics since the pioneering work by Sadi Carnot [1], and gained new momentum with the development of nonequilibrium thermodynamics of small-scale systems [2,3]. Unlike thermodynamics, fluctuations become fundamental at the nanoscale and the study of their role attracted large attention, both theoretically [4–7] and experimentally [8–10]. As irreversibility is unavoidable, the search for new strategies in the realm of nonequilibrium stochastic thermodynamics is crucial and strongly desirable. Bearing this in mind, several distinct approaches have been proposed. Among them, we highlight the study of the maximum attainable power [11–19] and efficiency [16,20], the modulation of the system-bath interaction time [21,22], and the dynamical control via shortcuts to adiabaticy [23–25] or isothermality [26].

The above examples deal with engines composed of a single or a few units. However, nature is plenty of complex systems composed of many interacting entities, in which cooperative effects often play a crucial role. Examples span multiple biological scales [27], from microbes [28] to the human brain [29], and have been studied in a broad range of research fields, from nonequilibrium effects in chemical processes [30–33] to synchronization in biological networks [34–38]. This vast spectrum of applications highlights that the demand for implementable and robust optimal strategies to engineer collective engines is important and timely. Although the interplay between collective effects and system's performances has been extensively studied in quantum systems [39–44], the development of classical setups built from interacting units is comparatively much less known and still remains at a primary stage [19,45–49].

We introduce a general class of collective engines, inspired by ferromagnetic equilibrium models [50–53]. They have a longstanding importance in the context of collective effects and are at the heart of numerous theoretical and experimental advances, having distinct models (e.g., the Ising, Potts, XY, and Heisenberg) as ideal platforms for describing ferromagnetism. Optimizing power and efficiency by changing driving and coupling parameters, we show that synchronized operations under ordered (ferromagnetic) arrangements play a central role in improving system performances. The main features and optimization routes of the engine proposed here can be unveiled both using a linear analysis close to equilibrium and an effective discrete-state model capturing all relevant effects. Finally, we highlight that our results are robust beyond the case of all-to-all interactions and pave the way for the building of promising nonequilibrium thermal machines based on ordered structures.

II. GENERAL MODEL AND THERMODYNAMICS

Since our goal is to investigate main features and advantages of the cooperative behavior emerging from ordered agents, we design a system composed of N all-to-all interacting units. Each unit can occupy q different states, so that a microstate i of the system is an N-dimensional vector containing the states of all units. This system is placed in contact with two baths at different temperatures ($\nu = 1$ is the cold one, $\nu = 2$ the hot) to work as a heat engine. Moreover,

*Corresponding author: busiello@pks.mpg.de

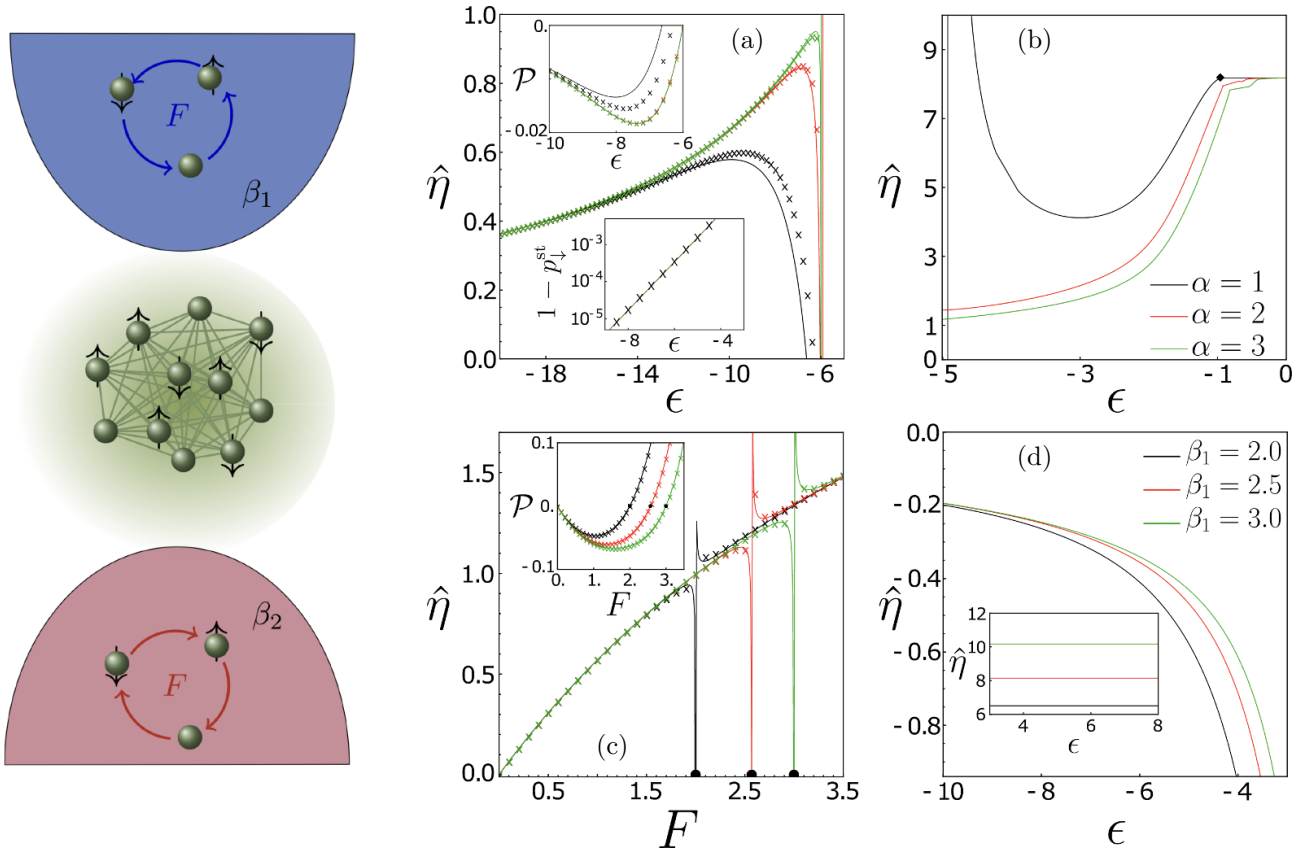

FIG. 1. (Left) Schematics of $q = 3$ engines. Arrows in the reservoirs indicate the direction of the driving F, which is clockwise at high temperature and counterclockwise at low temperature. (a) Model A ($\epsilon_{\downarrow\uparrow} \neq 0$). The efficiency $\hat{\eta} = \eta/\eta_c$ is shown for different α as a function of the coupling strength ϵ in the strong collective phase (smaller ϵ). Lines are exact results, while dots represents the effective model (see Sec. V). Power output per unit $\mathcal{P}$ is presented in the upper inset, while the lower inset is a semilog plot of $1 - p_{\downarrow}^{\rm st}$ to show the robustness of the effective description. (b) Same as (a), but in the presence of weak collective effects (larger ϵ). The symbol ♦ in (b) indicates the critical point ϵ_c separating the regimes of collective and independent units. As a result, collective ordered operations favor a heat engine behavior. Parameters in (a) and (b): $\beta_1 = 2$, $\beta_2 = 1$, and $F = 2$. (c) Model A. $\hat{\eta}$ and $\mathcal{P}$ (inset) vs F for different β_1. Vertical lines mark the crossover between heat engine and pump regimes, also indicated by •. Parameters in (c): $\alpha = 3$, $\epsilon = -6$, $\beta_2 = 1$. As previously, symbols correspond to the effective model. (d) Model B ($\epsilon_{\downarrow\uparrow} = 0$). For $F = 1$, $\beta_2 = 1$, and different β_1, the efficiency is shown as a function of ϵ, indicating only a dud regime in this case, as Ising-like interactions are absent. As ϵ increases, model B shows a pump behavior (inset).

worksources originate from γ_F distinct driving forces that also depend on the bath, i.e., $F_\gamma^{(\nu)}$ with $\gamma = 1, \ldots, \gamma_F$. In Fig. 1(a), we present a sketch of the model for $q = 3$. The dynamics of microstates is governed by the master equation

$$\dot{p}_j = \sum_{\nu=1}^{2} \sum_{i \neq j} \left(\omega_{ji}^{(\nu)} p_i - \omega_{ij}^{(\nu)} p_j \right),$$

$$\omega_{ji}^{(\nu)} = \Gamma e^{-\frac{\beta_\nu}{2}\{E_j - E_i + \sum_\gamma F_\gamma^{(\nu)} d_{\gamma,ji}^{(\nu)}\}},$$

where $\omega_{ji}^{(\nu)}$ is the transition rate from i to j due to the bath ν, and $d_{\gamma,ij}^{(\nu)}$ are antisymmetric coefficients associated with nonconservative driving (see Appendix A). Denoting by $N_\beta^{(i)}$, $\beta = 1, \ldots, q$, the occupation number of the state β in the microstate i, a transition to j leads to $N_\beta^{(j)} = N_\beta^{(i)} - 1$ and $N_{\beta'}^{(j)} = N_{\beta'}^{(i)} + 1$, where β and β' depend on initial and final microstates. The total energy E_i is given by the all-to-all expression

$$E_i = \sum_{\beta=1}^{q} \epsilon_\beta N_\beta^{(i)} + \frac{1}{2N} \sum_{(\beta,\beta'<\beta)}^{q} \left[\epsilon_{\beta\beta} N_\beta^{(i)} \left(N_\beta^{(i)} - 1 \right) + 2\epsilon_{\beta\beta'} N_\beta^{(i)} N_{\beta'} \right], \tag{1}$$

where ϵ_β, $\epsilon_{\beta\beta}$, and $\epsilon_{\beta\beta'}$ denote individual and interaction energies for units in the same and different states, respectively. The presence of $\epsilon_{\beta\beta'}$ makes the proposed model intrinsically more general than those proposed in [46,47] in the context of work-to-work converters.

From these preliminaries, the first law of thermodynamics is formulated from the time evolution of mean energy $\langle E \rangle = \sum_j E_j p_j$, which is given by $d\langle E \rangle/dt = \langle \mathsf{P} \rangle + \langle \dot{\mathsf{Q}}_1 \rangle + \langle \dot{\mathsf{Q}}_2 \rangle$, where the mean power $\langle \mathsf{P} \rangle$ and heat fluxes from the bath ν are

$$\langle \mathsf{P} \rangle = -\sum_{(\nu,\gamma)} F_\gamma^{(\nu)} \sum_{(i,j)} d_{\gamma,ji}^{(\nu)} J_{ji}^{(\nu)}, \tag{2}$$

$$\langle \dot{\mathsf{Q}}_\nu \rangle = \sum_{(i,j)} \left(E_j - E_i + \sum_\gamma F_\gamma^{(\nu)} d_{\gamma,ji}^{(\nu)} \right) J_{ji}^{(\nu)}, \tag{3}$$

expressed in terms of the probability current $J_{ij}^{(\nu)} = \omega_{ji}^{(\nu)} p_i - \omega_{ij}^{(\nu)} p_j$. The nonequilibrium steady state (NESS) is characterized by the probabilities $\{p_j^{\rm st}\}$ satisfying $\langle \dot{\mathsf{P}} \rangle + \langle \dot{\mathsf{Q}}_1 \rangle + \langle \dot{\mathsf{Q}}_2 \rangle = 0$ and associated with a positive entropy production into the environment $\langle \dot{\sigma} \rangle = -\beta_1 \langle \dot{\mathsf{Q}}_1 \rangle - \beta_2 \langle \dot{\mathsf{Q}}_2 \rangle$. Although exact, $\langle \dot{\sigma} \rangle$ can be further simplified when some channels are faster than others [54]. Employing the steady-state condition, $\langle \dot{\sigma} \rangle$ can be rewritten as $\langle \dot{\sigma} \rangle = \beta_1 \langle \dot{\mathsf{P}} \rangle + (\beta_1 - \beta_2) \langle \dot{\mathsf{Q}}_2 \rangle$, allowing us to characterize the engine performance through two (equivalent) definitions of efficiency, $\eta = -\langle \dot{\mathsf{P}} \rangle / \langle \dot{\mathsf{Q}}_2 \rangle$ and from the entropy production, $\hat{\eta} = -\eta_{\rm c}^{-1} \langle \dot{\mathsf{P}} \rangle / \langle \dot{\mathsf{Q}}_2 \rangle$, solely differing from each other for the Carnot bound $\eta_{\rm c} = 1 - \beta_2/\beta_1$. A heat engine partially converts the heat extracted from the hot thermal bath ($\langle \dot{\mathsf{Q}}_2 \rangle > 0$) into power output ($\langle \dot{\mathsf{P}} \rangle < 0$), hence exhibiting, by construction, a positive and bounded efficiency, $0 \leqslant \eta \leqslant \eta_c$ ($0 \leqslant \hat{\eta} \leqslant 1$). Conversely, the pump regime is characterized by an amount of work $\langle \dot{\mathsf{P}} \rangle > 0$, which is partially used to sustain a heat flux from the cold to hot bath, i.e., $\langle \dot{\mathsf{Q}}_2 \rangle < 0$, hence $\eta_c < \eta < \infty$ ($1 < \hat{\eta} < \infty$). Finally, for $\eta < 0$ the engine works in the so-called dud regime, i.e., the engine does not generate power.

To investigate the system's behavior, it is useful to map microstates i into occupation numbers $N_\beta^{(i)}$. To this aim, we need to perform a coarse-graining procedure (discussed below and in Appendix A). Then, the analysis will be first carried out for $N \to \infty$, deriving the evolution for the mean occupation density of the state β, $p_\beta = \langle \sum_i N_\beta^{(i)}/N \rangle$. Later on, we will extend it to finite N, studying how finite-size effects disappears to converge to a mean-field behavior. The thermodynamic quantities in the limit $N \to \infty$ are similar in form to those presented above for finite N. Indeed, the power $\mathcal{P}$ and heat $\langle \dot{Q}_\nu \rangle$ per unit are given by

$$\mathcal{P} = -\sum_{(\nu,\gamma)} F_\gamma^{(\nu)} \sum_{(\beta,\beta')} d_{\beta\beta'}^{(\nu)} J_{\beta\beta'}^{(\nu)},$$

$$\langle \dot{Q}_\nu \rangle = \sum_{(\beta,\beta')} \left(E_\beta - E_{\beta'} + \sum_\gamma F_\gamma^{(\nu)} d_{\beta\beta'}^{(\nu)} \right) J_{\beta\beta'}^{(\nu)}, \qquad (4)$$

with the energy difference $E_\beta - E_{\beta'}$ is the same quantity appearing also in the exponent of the transition rates in the mean-field approach (see Appendix A). Notice that, in Eq. (4), we use a different notation with respect to Eqs. (2) and (3) since these quantities are in general different due to the coarse-graining procedure [55–57].

III. MINIMAL ORDERED MODEL FOR COLLECTIVE HEAT ENGINES

In full generality, the expression of the energy in Eq. (1) presents a huge number of parameters to be considered, precisely $2q + q(q-1)/2$. For the sake of simplicity, we restrict our analysis to the cases $q = 2$ and $q = 3$, which can be respectively mapped into spin models $S = 1/2$, $\beta = \{\downarrow, \uparrow\}$, and $S = 1$, $\beta = \{\downarrow, 0, \uparrow\}$. We also consider two choices for the interaction parameters $\epsilon_{\beta\beta'}$, inspired by two cornerstones in statistical physics, Ising and Potts models [50,58], here respectively named model A and B, for clarity. Hence, in model A with $q = 3$, we take $\epsilon_{\uparrow\uparrow} = \epsilon_{\downarrow\downarrow} = \epsilon$, $\epsilon_{\uparrow\downarrow} = -\alpha\epsilon$, and

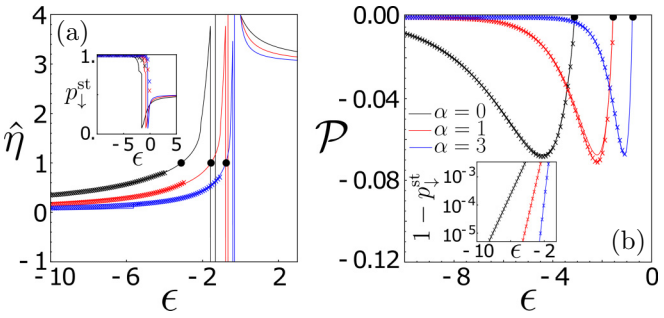

FIG. 2. $q = 2$ engine (model A). For $\beta_1 = 2$, $\beta_2 = F = 1$, and distinct α, panels (a) and (b) respectively show the efficiency $\hat{\eta}$ and the power per unit $\mathcal{P}$ vs the interaction strength ϵ. Black circles indicate the optimal efficiency, $\eta_{\rm ME} = \eta_c$ ($\hat{\eta}_{\rm ME} = 1$) in this setting (see Sec. IV). Symbols correspond to the effective two-state description, presented in Sec. V. Insets: Plot of $p_\downarrow^{\rm st}$ (a) and semilog plot $p_\uparrow^{\rm st}$ (b) vs ϵ.

$\epsilon_{\uparrow 0} = \epsilon_{\downarrow 0} = \epsilon_{00} = 0$, with $\epsilon_{\beta\beta'}$ symmetric for every β, β'. Here, α tunes the interaction strength between units in different states. Conversely, model B is defined by $\epsilon_{\beta\beta'} = \epsilon\delta_{\beta,\beta'}$, with no interaction between units in different states, resembling the setting employed in [46,47]. We always consider the self-interaction terms ϵ_β to be all equal. In analogy to other engine setups [45,46], and also compatibly with models of biochemical motors, such as kinesin [59,60], photo-acids [61,62], and ATP-driven chaperones [63,64], the worksource is implemented by introducing a bias for the occurrence of certain transitions, forcing, in this context, each unit to rotate in its state-space (see Figs. 1 and 2 for $q = 3$ and $q = 2$, respectively). Practically, this bias is realized by setting $d_{\gamma,ij}^{(\nu)} = (-1)^\nu$ if the transition from j to i is clockwise, where the opposite rate is determined by the antisymmetric property. We further simplify the system by taking $\Gamma = 1$ and only one kind of driving, i.e., $\gamma_F = 1$ and $F^{(\nu)} = F$ for both ν.

Figure 1 shows the main features of model A and B for $q = 3$ and $N \to \infty$, in which $p_\beta^{\rm st} \in \{p_\uparrow^{\rm st}, p_\downarrow^{\rm st}, p_0^{\rm st}\}$. In such a mean-field limit, the system is described by a nonlinear master equation that cannot be self-consistently solved (see Appendix A). In Figs. 1(a) and 1(b), we show efficiency and power output per unit for model A. This setting allows for the existence of a collective ordered phase for large negative ϵ. In this regime, the system behaves as a heat engine [see Fig. 1(a)]. As ϵ increases, units deviate from a synchronized phase and a pump behavior emerges. For $\alpha = 1$, units starts operating independently after a phase transition, indicated by ♦ in Fig. 1(b), while for other α there is a crossover between these collective and independent regimes. Moreover, Fig. 1(c) shows that F can be used as a parameter to control the system, as when F increases a pump behavior emerges even in the collective ordered phase. As shown below in Sec. VIII, power and heat fluxes are independent from ϵ when units operate independently, indicating that, in the collective phase, ϵ can be chosen appropriately to lead to a better performance even as a pump and hence hinting at the relevance of a synchronous phase for this class of engines. Conversely, no heat regime is present for model B [see Fig. 1(d)], when only Potts-like interactions are present. If units operate independently, the

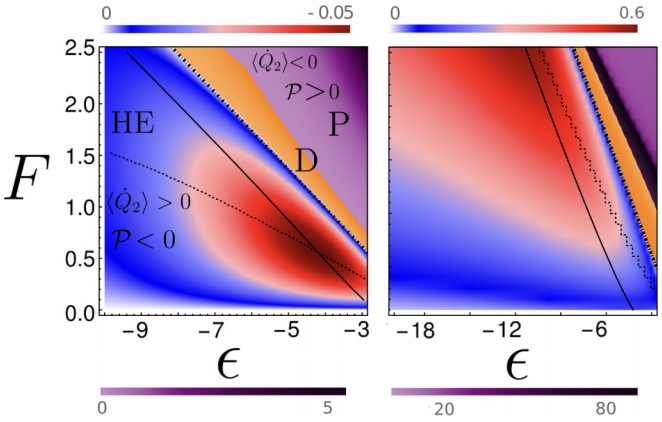

FIG. 3. Model A and $q = 3$. Left panel depicts the power heat map as a function of driving F and coupling ϵ. HE, P, and D indicate, respectively, heat engine, pump, and dud regimes. The solid line shows the maximum power with respect to F at fixed ϵ, while the dashed line accounts for the maximization with respect to ϵ. These two lines cross at the global maximum power. Right panel shows the efficiency $\hat{\eta}$ heat map as a function of F and ϵ. Solid and dashed lines again indicate maximization with respect to F and ϵ, respectively. In both panels, the dot-dashed lines only indicate the boundaries of heat engine regimes. Parameters: $\beta_1 = 2$, β_2=1, α=1.

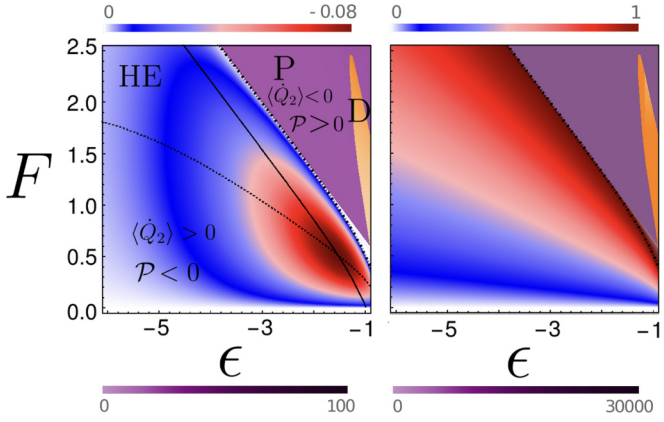

FIG. 4. Heat maps for $\mathcal{P}$ and $\hat{\eta}$ for the same parameters as in Fig. 2. Heat engine, pump, and dud regimes are described by symbols HE, P, and D, respectively. Continuous and dotted lines denote the maximization of power respectively holding F and ϵ fixed. The dot-dashed line corresponds to the crossover from heat engine to pump regimes, in which $\eta = \eta_c$ in this setup ($q = 2$).

engine can only work as a pump in this case. Although model B has been proposed as a work-to-work converter, exhibiting maximum power in the collective regime [46], the absence of Ising-like interactions makes the synchronous phase useless to operate as a heat engine. For these reasons, model A will be used as reference model from now on. Analogous findings are also reported for $q = 2$ (model A) in Fig. 2. Indeed, we show the efficiency $\hat{\eta}$ and the power per unit $\mathcal{P}$ as a function of the interaction strength ϵ for different α's, highlighting the presence of the transition from heat engine to pump regime.

IV. OPTIMIZING POWER AND EFFICIENCY

To investigate the optimal working regimes of the proposed model, we extend our results to a wider spectrum of values of the coupling parameter ϵ and the driving F. Figures 3 and 4 show the resulting heat maps again for $q = 3$ and $q = 2$ (model A), respectively. Heat engine (blue-red) and pump (purple) regimes are separated by an intermediate region in which units operate dudly (orange). Power and efficiency can be optimized with respect to F (solid lines) or ϵ (dashed lines), where the other quantity is held fixed. It is worth noting that the power output in the heat engine regime presents a global maximum where the two optimization lines cross (dark red spot). This point coincides with the power obtained by simultaneous optimization with respect to F and ϵ. Conversely, no optimal point exists for the efficiency in the (F, ϵ) space, and the heat engine operates more efficiently as $|\epsilon|$ and F are increased. This result hints at the possibility to boost the performance of a stochastic heat engine by favoring the emergence of collective order. We highlight that, when $q = 2$ (and $\alpha = 1$), the system exhibits a qualitatively similar behavior with respect to the case $q = 3$.

As suggested by Fig. 1, an alternative route for optimization prescribes, at finite ϵ and F, to increase the value of the coupling between different states α. In Fig. 5, we show the maximum efficiency $\eta_{\rm ME}$, the efficiency at maximum power $\eta_{\rm MP}$, and the one obtained by simultaneous optimization $\eta^*_{\rm MP}$, as a function of α for model A and $q = 3$. It is worth noting that $\eta_{\rm ME}$ approaches (and eventually reaches) the ideal Carnot efficiency η_c, while $\eta^*_{\rm MP}$ saturates the Curzon-Ahlborn bound, $\eta_{CA} = 1 - \sqrt{\beta_2/\beta_1}$, as the coupling strength is increased. Furthermore, the efficiency at maximum power lies between these two bounds: $\eta_{CA} < \eta_{\rm MP} < \eta_c$. It is worth noting that, for $q = 2$, the Carnot efficiency is reached for all values of α provided that $\mathcal{P} = \langle \dot{Q}_2 \rangle = 0$, as also shown by black circles in Fig. 2. Together with the results presented in the heat maps, we can state that, considering a general interacting model admitting an ordered phase, the performance as a heat engine

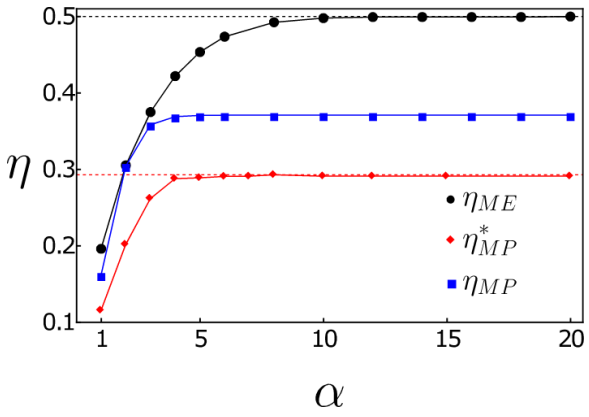

FIG. 5. Maximum efficiency $\eta_{\rm ME}$ (black circles), efficiency at maximum power $\eta_{\rm MP}$ (blue squares), and efficiency at global maximum power $\eta^*_{\rm MP}$ (red diamonds), as a function of the coupling between different states α. Solid lines are guides for the eye. The black and red dashed lines correspond Carnot η_c and Curzon-Ahlborn η_{CA} efficiencies, respectively.

benefits from a synchronized behavior, in combinations with the presence of Ising-like couplings.

V. EFFECTIVE DESCRIPTION IN THE REGIME OF STRONG COLLECTIVE EFFECTS

Despite being exact in all cases, the nonlinear form of the master equation prevents the derivation of closed expressions for probabilities and clear insights about the influence of each parameter. To grasp the main features of the system in the regime of strong collective effects, we develop an effective discrete-state description, which is valid in the ordered collective regime. By taking $\alpha > 0$, $\epsilon < 0$, and $-\epsilon \gg F > 0$, this effective description can be derived employing the matrix-tree theorem [65]. We start describing the system as a coarse-grained q-state model. Starting with $q = 2$ to fix the ideas, the ordered phase is twofold degenerate and characterized by the predominance of spins of one type ($\downarrow$ or $\uparrow$). As a consequence, a two-state system exhibiting collective order can only be in two states, $\downarrow$ or $\uparrow$. It can be described using a coarse-grained master equation with two transition channels, i.e., driven by bath 1 or 2. The form of the steady-state solution is

$$p_{\downarrow}^{st} \approx \frac{\omega_{\downarrow\uparrow}^{(1)} + \omega_{\downarrow\uparrow}^{(2)}}{\omega_{\downarrow\uparrow}^{(1)} + \omega_{\downarrow\uparrow}^{(2)} + \omega_{\uparrow\downarrow}^{(1)} + \omega_{\uparrow\downarrow}^{(2)}} . \tag{5}$$

The explicit expression of the transition rates is shown in Appendix A. Equation (5) is an implicit equation, as transition rates depend on $p_{\downarrow}$. By focusing on the case $p_{\downarrow}^{st} \approx 1$ (the other opposite case can be immediately obtained by swapping $\downarrow$ with $\uparrow$), and performing the $\epsilon \to -\infty$ limit, we have

$$p_{\downarrow}^{st} \approx \frac{1}{1 + e^{\frac{1}{2}\{(\beta_1+\beta_2)(\alpha+1)\epsilon + F(\beta_1-\beta_2)\}}} . \tag{6}$$

Taking into account that $\beta_2 < \beta_1$, $F > 0$ and $-\epsilon \gg F$, as we are in the regime of strong collective effects, we can approximate the above expression as $p_{\downarrow}^{st} \approx \frac{1}{2} e^{\{(\beta_1+\beta_2)(1+\alpha)\epsilon\}} e^{\frac{(\beta_1-\beta_2)F}{2}}$. This can also be derived from the fact that $p_{\downarrow}^{st} \approx 1 - (\omega_{\uparrow\downarrow}^{(1)} + \omega_{\uparrow\downarrow}^{(2)})/(\omega_{\downarrow\uparrow}^{(1)} + \omega_{\downarrow\uparrow}^{(2)}) \approx 1 - \omega_{\uparrow\downarrow}^{(1)}/\omega_{\downarrow\uparrow}^{(2)}$, under the aforementioned assumptions. By inserting the approximate expression for $p_{\downarrow}^{st}$ into the formulas in Eq. (4), one arrives at the following expression for the effective power per unit, $\mathcal{P}_{\text{eff}}$ when $q = 2$:

$$\mathcal{P}_{\text{eff}} = \frac{F}{2} e^{-\frac{1}{2}\beta_2[(\alpha+1)\epsilon M + F]} \Big[e^{\frac{1}{2}[(\beta_1+\beta_2)F - (\beta_1-\beta_2)(\alpha+1)\epsilon M]} - 1 \Big] \times \Big[(1+M) e^{\frac{1}{2}[-(\beta_1-\beta_2)F + (\beta_1+\beta_2)(\alpha+1)\epsilon M]} - M + 1 \Big].$$

Analogously, we obtain the following expression for the effective heat flux from the bath 2, $\langle \dot{Q}_2 \rangle_{\text{eff}}$:

$$\langle \dot{Q}_2 \rangle_{\text{eff}} = -(F + (\alpha+1)M\epsilon) \left[\sinh\left(\frac{\beta_2}{2}(F + (\alpha+1)M\epsilon) \right) + M \cosh\left(\frac{\beta_2}{2}(F + (\alpha+1)M\epsilon) \right) \right],$$

with $M = p_{\downarrow}^{\text{st}} - p_{\uparrow}^{\text{st}}$ is the order parameter. It is worth mentioning that $|M|$ reduces to $1 - 2e^{\beta(1+\alpha)\epsilon}$ in the equilibrium regime ($\beta_1 = \beta_2$ and $F = 0$), becoming equal to the magnetization per spin of the Ising model for sufficiently low temperatures $\beta \gg \beta_c = (1+\alpha)\epsilon/k_B$. Figure 2 shows the validity of our approximate expressions for $p_{\downarrow}^{st}$ for distinct sets α when $q = 2$ (symbols in the figure).

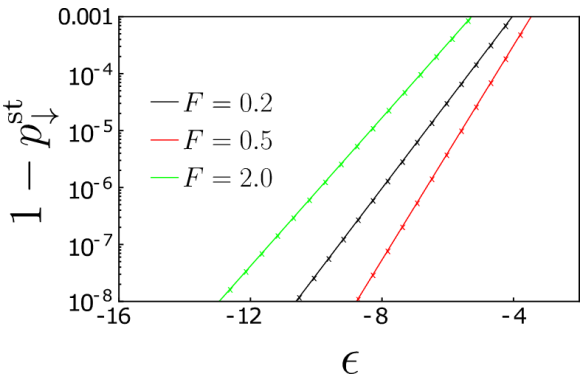

FIG. 6. Model A, $q = 3$. Semilog plot of $1 - p_{\downarrow}^{\text{st}}$ vs ϵ for distinct sets of β_1 and F. Continuous lines are exact results for $N \to \infty$, while symbols corresponds to the solution evaluated from the effective model. Black, red, and green curves show results for $\beta_1 = 5/2$, $10/3$ and 2, respectively. In all cases $\beta_2 = 1$.

Our effective description can be employed also when $q = 3$, always considering model A. First, we consider the coarse-grained three-state system, where each state corresponds to a spin state. Then, directly from the transition rates, we observe that, when the system is in one of the degenerate collective states, say $\downarrow$, i.e., $p_{\downarrow}^{st} \approx 1$, the transitions from $\uparrow$ to $\downarrow$ and 0 are almost unidirectional for $F > 0$ and $-\epsilon \gg F$. As a consequence, we can approximate the coarse-grained three-state system as a two-state model with only 0 and $\downarrow$. Finally, we deal with this system following the same steps as in the $q = 2$ scenario, obtaining

$$p_{\downarrow}^{st} \approx \frac{1}{1 + e^{\frac{1}{2}\{(\beta_1+\beta_2)\epsilon + (\beta_1-\beta_2)F\}}} , \tag{7}$$

with $p_0^{st} \approx 1 - p_{\downarrow}^{st}$. Once again, as before, we can also write $p_{\downarrow}^{st} \approx 1 - \omega_{0\downarrow}^{(1)}/\omega_{\downarrow 0}^{(2)} = 1 - e^{\frac{1}{2}\{(\beta_1+\beta_2)\epsilon + (\beta_1-\beta_2)F\}}$, which gives our approximation for strong collective effects. Figure 6 shows the validity of our approximate expressions for $p_{\downarrow}^{st}$ for distinct sets of temperatures β_1, β_2, and F, when $q = 3$.

The corresponding expression for power per unit is given by

$$\mathcal{P}_{\text{eff}} = F\Big[(1+M)\big(e^{\frac{\beta_1}{2}\Phi_-^{(\alpha)}} - e^{-\frac{\beta_2}{2}\Phi_+^{(\alpha)}} - e^{-\frac{\beta_1}{2}\Phi_-} + e^{\frac{\beta_2}{2}\Phi_+} \big) - M\big(e^{\frac{\beta_1}{2}\Phi_-} - e^{-\frac{\beta_2}{2}\Phi_+} - e^{-\frac{\beta_1}{2}(\Phi_+^{(\alpha)} + M\epsilon)} + e^{\frac{\beta_2}{2}(\Phi_-^{(\alpha)} - M\epsilon)} \big) \Big], \tag{8}$$

where $\Phi_\pm = F \pm M\epsilon$ and $\Phi_\pm^{(\alpha)} = F \pm \alpha M\epsilon$, with $M = p_{\downarrow}^{st} - p_{\uparrow}^{st} \approx 1 - e^{\frac{1}{2}\{(\beta_1+\beta_2)\epsilon + (\beta_1-\beta_2)F\}} > 0$. Also in this case, from Eq. (4), we obtain the following expression for $\langle \dot{Q}_2 \rangle_{\text{eff}}$:

$$\langle \dot{Q}_2 \rangle_{\text{eff}} = -(1+M)\big[\Phi_+ e^{\frac{1}{2}\beta_2\Phi_+} - \Phi_+^{(\alpha)} e^{-\frac{1}{2}\beta_2\Phi_+^{(\alpha)}} \big] + M\big[(\Phi_-^{(\alpha)} - M\epsilon) e^{\frac{1}{2}\beta_2(\Phi_-^{(\alpha)} - M\epsilon)} - \Phi_+ e^{-\frac{1}{2}\beta_2\Phi_+} \big]. \tag{9}$$

The efficiency is readily evaluated taking their ratio. In the limit of large α, it reads

$$\eta_{\rm eff} = \frac{F}{\Phi_+}\left[1 - \frac{\exp\left(-\frac{\beta_1}{2}\Phi_-\right) + 2M\cosh\left(\frac{\beta_1}{2}\Phi_-\right)}{\exp\left(\frac{\beta_2}{2}\Phi_+\right) + 2M\cosh\left(\frac{\beta_2}{2}\Phi_+\right)}\right]. \quad (10)$$

The validity of this approach is also shown in Fig. 1 for different values of α (symbols). The effective discrete-state model provides a very good description of both the heat engine and pump regimes. However, small discrepancies arise when $p^{st}_{\uparrow}$ is not negligible (e.g., for small $-\epsilon$ and F).

VI. LINEAR THERMODYNAMICS

The main features of the system proposed here can also be investigated through a linear analysis close to equilibrium, e.g., $\beta_1 - \beta_2 \ll 1$ and $F \ll 1$. By resorting to the ideas of linear stochastic thermodynamics [16,66–69], we introduce the following thermodynamic forces $f_1 = \beta_1 - \beta_2$ and $f_2 = \beta_1 F$, in such a way that the entropy production $\langle\dot{\sigma}\rangle$ is expressed in the bilinear form

$$\langle\dot{\sigma}\rangle = (\beta_1 - \beta_2)\langle\dot{Q}_2\rangle + \beta_1\mathcal{P} = J_1 f_1 + J_2 f_2, \quad (11)$$

where $J_1 = \langle\dot{Q}_2\rangle$ and $J_2 = \mathcal{P}/F$ denote the thermodynamic fluxes. Such fluxes can be expressed in terms of the Onsager coefficients, $J_1 = L_{11}f_1 + L_{12}f_2$ and $J_2 = L_{21}f_1 + L_{22}f_2$, which satisfy the conditions $L_{11}, L_{22} \geqslant 0$ and $L_{12} = L_{21}$. From the equation above, the efficiency $\hat{\eta}$ promptly reads

$$\hat{\eta} = -\frac{\beta_1\mathcal{P}}{(\beta_1 - \beta_2)\langle\dot{Q}_2\rangle} = -\frac{L_{21}f_2f_1 + L_{22}f_2^2}{L_{11}f_1^2 + L_{12}f_1f_2}, \quad (12)$$

from which $\eta = \hat{\eta}\,\eta_c$ follows immediately. As previously, heat engine ($\mathcal{P} < 0$) and pump ($\mathcal{P} > 0$) regimes impose boundaries to the optimization with respect to f_2, whose absolute value must lie in the interval $0 \leqslant |f_2| \leqslant |f_m|$, where $f_m = -L_{21}f_1/L_{22}$, i.e., the so-called stopping force for which $\mathcal{P} = 0$. As previously, the optimization can be performed to obtain maximum power $\mathcal{P}_{\rm MP}$ (with efficiency $\eta_{\rm MP}$) or maximum efficiency $\eta_{\rm ME}$ (with power $\mathcal{P}_{\rm ME}$), by changing the force f_2 to optimal values $f_{2,\rm MP}$ and $f_{2,\rm ME}$, respectively. These optimal output forces can be expressed in terms of the Onsager coefficients as

$$f_{2,\rm ME} = \frac{L_{11}}{L_{12}}\left(-1 + \sqrt{1 - \frac{L_{12}^2}{L_{11}L_{22}}}\right)f_1, \quad (13)$$

and

$$f_{2,\rm MP} = -\frac{1}{2}\frac{L_{12}}{L_{22}}f_1, \quad (14)$$

respectively, where the property $L_{21} = L_{12}$ has been considered. By inserting $f_{2,\rm ME}$ or $f_{2,\rm MP}$ into the expression for $\hat{\eta}$, we obtain $\hat{\eta}_{\rm ME}$ and the efficiency at maximum power $\hat{\eta}_{\rm MP}$ given by

$$\hat{\eta}_{\rm ME} = -1 + \frac{2L_{11}L_{22}}{L_{12}^2}\left(1 - \sqrt{1 - \frac{L_{12}^2}{L_{11}L_{22}}}\right), \quad (15)$$

and

$$\hat{\eta}_{\rm MP} = \frac{L_{12}^2}{4L_{11}L_{22} - 2L_{12}^2}. \quad (16)$$

Similarly, we can derive the expressions for $\mathcal{P}_{\rm MP}$ and $\mathcal{P}_{\rm ME}$. All these quantities are not independent of each other, instead they satisfy the following relationships:

$$\hat{\eta}_{\rm MP} = \frac{\hat{\eta}_{\rm ME}}{1 + \hat{\eta}_{\rm ME}^2} \quad \text{and} \quad \frac{\mathcal{P}_{\rm ME}}{\mathcal{P}_{\rm MP}} = 1 - \hat{\eta}_{\rm ME}^2, \quad (17)$$

where the symmetry between crossed Onsager coefficients $L_{12} = L_{21}$ has been taken into account. It is convenient to introduce the *coupling parameter* $\kappa = L_{12}/\sqrt{L_{11}L_{22}}$ [12,70], in such a way that optimal efficiencies $\hat{\eta}_{\rm MP}$ and $\hat{\eta}_{\rm ME}$ are solely expressed in terms of this quantity as follows:

$$\hat{\eta}_{\rm ME} = -1 + \frac{2}{\kappa^2}(1 - \sqrt{1 - \kappa^2}), \quad (18)$$

and

$$\hat{\eta}_{\rm MP} = \frac{1}{2}\frac{\kappa^2}{2 - \kappa^2}, \quad (19)$$

respectively. Since $\langle\dot{\sigma}\rangle \geqslant 0$, it follows that κ must be constrained in the interval $-1 \leqslant \kappa \leqslant 1$, implying that both $\hat{\eta}_{\rm MP}$ and $\hat{\eta}_{\rm ME}$ are confined to $0 \leqslant \hat{\eta}_{\rm MP} \leqslant 1/2$ and $0 \leqslant \hat{\eta}_{\rm ME} \leqslant 1$, respectively. Notice that $\kappa = \pm 1$ implies that the determinant of the (2×2) Onsager matrix is equal to zero. This, in turn, implies proportionality between the two thermodynamic fluxes, i.e., $J_1 \propto J_2$, for all forces f_1 and f_2. Figure 7 shows that all the signatures about collective effects are also captured by the linear regime, describing very well the system behavior near the equilibrium regime [panels (b) and (c)]. Remarkably, the increase of efficiencies towards the Carnot bound as ϵ and F increase, as described in the main text, is understood from the interplay among Onsager coefficients L_{ij} [shown in panel (a) as a function of ϵ], that leads to $\kappa \to -1$ (inset of panel (d)). Also, $\hat{\eta}_{\rm ME}$ and $\hat{\eta}_{\rm MP}$ closely follow the analytical expressions presented in Eqs. (18) and (19) [see Fig. 7(d)]. Since $|\kappa|$ monotonically increases with ϵ, both $\eta_{\rm ME}$ and $\eta_{\rm MP}$ approach to their ideal values when collective ordered effects are stronger, highlighting the importance of unit synchronization to increase engine performance.

As a last comment, it is worth pointing out there is no a-priori advantage for the system when operating near criticality. Since κ, i.e., a measure of the degree of collective effects, vanishes as the system approaches to the criticality (as ϵ increases), both $\hat{\eta}$ and power $\mathcal{P}$ also decreases [see Fig. 7(d)]. This is also consistent with Eqs. (15) and (16).

VII. MANY VERSUS FEW INTERACTING UNITS AND BEYOND THE ALL-TO-ALL CASE

Although our findings have been derived in the $N \to \infty$ limit for all-to-all interactions, the main hallmarks have found to be robust when finite-size effects and other topologies are considered. Figures 8(a) and 8(b) show, for model A and $q = 3$, numerical results for the all-to-all case at increasing N. We notice a reduced range of parameters for which the system operates as a heat engine, but no significant qualitative changes. In Appendix B, we also explore the limiting case $N = 2$ and

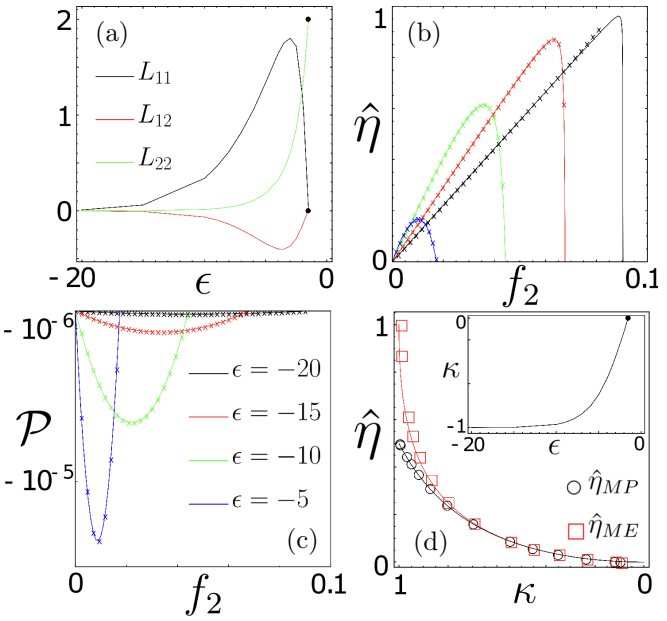

FIG. 7. For model A, $q = 3$ and $\alpha = 1$, we show the thermodynamics of the system close to the equilibrium regime. Panel (a) show the Onsager coefficients L_{ij} vs the interaction parameter ϵ. In (b) and (c), respectively $\hat{\eta}$ and $\mathcal{P}$ vs f_2 are reported for $f_1 = 9 \times 10^{-3}$. Continuous lines are exact results, while symbols correspond to Eq. (12). The heat engine behavior is delimited by $f_2 = f_m$. Panel (d) shows the behavior of maximum efficiency $\hat{\eta}_{\rm ME}$ and efficiency at maximum power $\hat{\eta}_{\rm MP}$ vs κ, where continuous lines follow Eqs. (18) and (19). The inset show how κ changes as a function of ϵ, and • denotes the phase transition to the independent regime taking place at $\epsilon_c \approx -1.5$ [see also the same symbol in (a)].

we find similar results, showing that a minimal setup of $N = 2$ interacting units already captures the essential ingredients of the model. It is worth noting that the system starts approaching

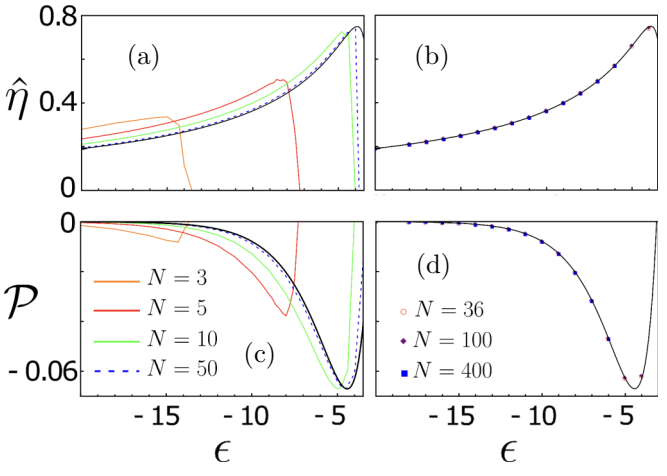

FIG. 8. (a) Efficiency $\hat{\eta}$ in the heat engine regime for increasing system size N. The black continuous line represents the case $N \to +\infty$. (b) The all-to-all case (continuous line) is compared with a square lattice of increasing size $N = L^2$ (dots). (c) Same as (a) for the power output per unit $\mathcal{P} = \langle \mathrm{P} \rangle / N$. (d) Same as (b) for $\mathcal{P}$. Numerical values have been obtained through Gillespie algorithm. Parameters: $\beta_1 = 2$, $\beta_2 = 1$, $F = 1$, and $\alpha = 3$.

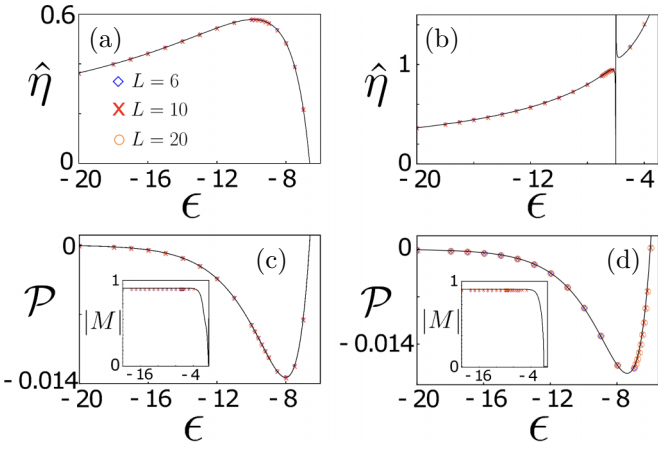

FIG. 9. Performance of model A for $q = 3$ on a square lattice of linear size L ($k = 4$ nearest neighbors). (a) Efficiency $\hat{\eta}$ as a function of ϵ for $\alpha = 1$, in the presence of a discontinuous transition between heat engine and pump regime. (b) Efficiency as a function of ϵ for $\alpha = 3$, in the presence of a crossover behavior. (c) Power output per unit $\mathcal{P}$ as a function of ϵ for $\alpha = 1$. The inset shows the behavior of $|M|$ with ϵ. (d) $\mathcal{P}$ as a function of ϵ for $\alpha = 3$. The inset shows the order parameter as a function of ϵ. In all panels, symbols indicate numerical results for the system size $N = L^2$, while continuous lines the all-to-all case. Parameters: $\beta_1 = 2$, $\beta_2 = 1$, $F = 2$. Numerical results have been obtained through Gillespie algorithm.

the mean-field behavior already for $N \geqslant 10$, in similarity to work-to-work transducers [46]. A very interesting feature is an increase in the finite-size efficiency at small ϵ, due to the fact that $\langle \dot{\mathrm{Q}}_2 \rangle / N$ monotonically decreases with N, while the absolute value of $\mathcal{P} = \langle \mathrm{P} \rangle / N$ increases within a certain range of parameters.

The all-to-all case also remarkably describes very precisely the behavior of interactions forming a regular arrangement. We restrict, for simplicity, our analysis to model A and $q = 3$ in a square lattice of linear size L. Each site i is associated with a spin variable $\sigma_i = \pm 1, 0$ and Eq. (1) then becomes

$$E_i = \frac{1}{2k} \sum_{i=1}^{N} \sum_{j=1}^{k} \epsilon \sigma_i \sigma_{i+j} \left[\delta_{\sigma_i, \sigma_{i+j}} + \alpha \delta_{\sigma_i, -\sigma_{i+j}} \right], \qquad (20)$$

where $k = 4$ for the square lattice. Despite the absence of exact results in such case, system's behavior and thermodynamic properties can be evaluated numerically by employing the Gillespie algorithm [71]. In panels (c) and (d) of Fig. 8 and in Fig. 9, we draw distinct comparisons with the all-to-all case, for distinct parameters and by increasing the system size. All of them agree almost perfectly, highlighting that the all-to-all case is insightful also when considering lattice models. This observation not only reinforces the generality of the model proposed here to grasp the interplay between collective effects and system's performance, but also the reliability of our results for finite-size systems.

VIII. CROSSOVER FROM HEAT ENGINE TO PUMP REGIMES

Figure 10 depicts the relationship between synchronization degree and system efficiency $\hat{\eta}$ for the same parameters as

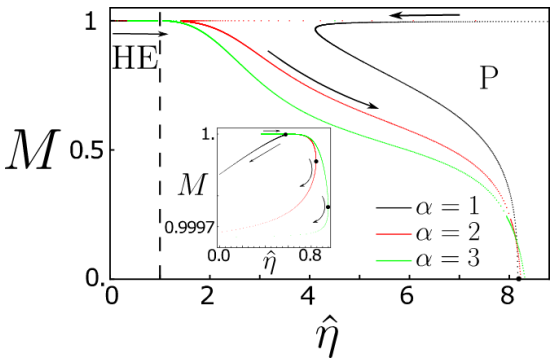

FIG. 10. For the same parameters of Fig. 1(a), we show the order parameter $M = p_{\downarrow}^{st} - p_{\uparrow}^{st}$ vs system efficiency $\hat{\eta}$ for collective (HE, i.e., heat engine) and independent (P, i.e., pump) regime. (Inset) Zoom of the curves in the heat engine regime, • indicates where the maximum value of efficiency is attained. Arrows represent the direction of increasing ϵ.

in Fig. 1. This result is consistent with the fact that the system operates as a heat engine and pump respectively when units operate collectively and almost (or completely) independently. In all cases, as ϵ increases towards positive values (arrows in Fig. 10), the system hits a threshold ϵ_c giving rise to the independent mode operations. This threshold can emerge in different ways, such as via a discontinuous phase transition ($q = 2$, model A and B; $q = 3$, model B) or a continuous one ($q = 3$, model A, $\alpha = 1$), or even as a crossover with no phase transitions ($q = 3$, model A, $\alpha \neq 1$). Although our general findings are valid in all cases, in the presence of a phase transition it is possible to obtain closed expression for $\mathcal{P}$ and $\langle \dot{Q}_\nu \rangle$ per unit. As shown in Appendix C, the disordered regime in such cases is characterized by equal probabilities $p_{\downarrow}^* = p_0^* = p_{\uparrow}^* = 1/3$ for $\epsilon \geqslant \epsilon_c$. By inserting this condition into Eq. (4), it follows that

$$\mathcal{P} = 2F\left[\sinh\left(\frac{F\beta_1}{2}\right) + \sinh\left(\frac{F\beta_2}{2}\right)\right] \quad \text{and}$$
$$\langle \dot{Q}_\nu \rangle = -2F \sinh\left(\frac{F\beta_\nu}{2}\right), \tag{21}$$

both being independent on ϵ. Similar formulas can be obtained for $q = 2$ and $\epsilon \to \infty$, solely differing from them by a factor 2. The corresponding efficiency, in both cases, is $\eta = 1 + (\sinh(\beta_1 F/2)/\sinh(\beta_2 F/2))^{-1}$. All these expressions state that only a pump regime is possible when units operate independently. Although both collective and independent operations allow the emergence of a pump regime, power and heat fluxes are independent from ϵ when units operate independently, Eq. (21), indicating that, in the collective phase, ϵ can be chosen appropriately to lead to a better performance even as a pump. This result strengthen further the role of interactions and collective operations in an engine model with Ising-like interactions.

IX. CONCLUSIONS

We introduced a minimal class of reliable thermal engines composed of several interacting units. We showed that, when they operate in a synchronized way, the engine can exhibit distinct regimes, along with maximal powers and efficiencies, in stark contrast to what happens when units operate independently. Despite the nontrivial interplay between interactions, driving, and collective effects, all main features can be captured using linear analysis and a discrete-state effective model, which proved to be very useful to characterize these engines. Our results clearly show the importance of a collective ordered phase to have powerful stochastic heat engines. The overall approach presented here is very general and opens the door to exciting directions for future research. First, the extension to different network topologies might be important not only to build more realistic and possibly more efficient setups, but also to check the robustness of these results, obtained in the case of all-to-all interactions, when the couplings are more sparse. Furthermore, it will be interesting to draw a comparison with other stochastic engine models, such as the sequential ones, in which the system is subjected to distinct conditions for different time periods and not simultaneously. Finally, a very fascinating open question remains to set universal bounds for power, efficiency, and dissipation, possibly expressed in terms of interaction parameters and strength of collective effects. They might provide important insights about the importance of synchronized operations to boost the performance of interacting systems in different contexts, from biochemical engines [72–74] to information processing [75,76].

ACKNOWLEDGMENTS

This study was supported by the Special Research Fund (BOF) of Hasselt University under Grant No. BOF23BL14. Authors are grateful to Pedro Harunari for useful suggestions and comments. This work has received the financial support from FAPESP under Grants No. 2021/03372-2 and No. 2021/13287-2. We also acknowledge CAPES and CNPq for financial support.

APPENDIX

Appendixes are structured as follows: In Appendix A we describe the transition rates for finite N and $N \to \infty$ interacting units. Appendix B depicts the thermodynamic quantities for the minimal setup composed of $N = 2$ interacting unities. As an additional investigation, the linear stability of the disordered solution for $q = 3$ is investigated in Appendix C.

APPENDIX A: TRANSITION RATES

As stated in the main text, collective effects from ordered structures have been investigated for two models (A and B), for $q = 2$ and $q = 3$. When $q = 2$, model B can be derived from model A setting $\alpha = 0$. The system dynamics is governed by the master equation $\dot{p}_j = \sum_{\nu=1}^{2} \sum_{i \neq j} (\omega_{ji}^{(\nu)} p_i - \omega_{ij}^{(\nu)} p_j)$, where the transition rates from i to j are given by

$$\omega_{ji}^{(1)} = \Gamma e^{-\frac{\beta_1}{2}\{\mp\epsilon(1+\alpha)(1-\frac{2N_{i\uparrow(\downarrow)}\mp 1}{N})\mp F\}} \quad \text{and}$$
$$\omega_{ji}^{(2)} = \Gamma e^{-\frac{\beta_2}{2}\{\mp\epsilon(1+\alpha)(1-\frac{2N_{i\uparrow(\downarrow)}\mp 1}{N})\pm F\}}, \tag{A1}$$

where the sign of $\mp\epsilon(1+\alpha)$ accounts for the fact that $N_{\uparrow}^{(j)} = N_{\uparrow}^{(i)} \pm 1$ and $N_{\downarrow}^{(i)} = N_{i\downarrow} \mp 1$. Analogously, the sign of the

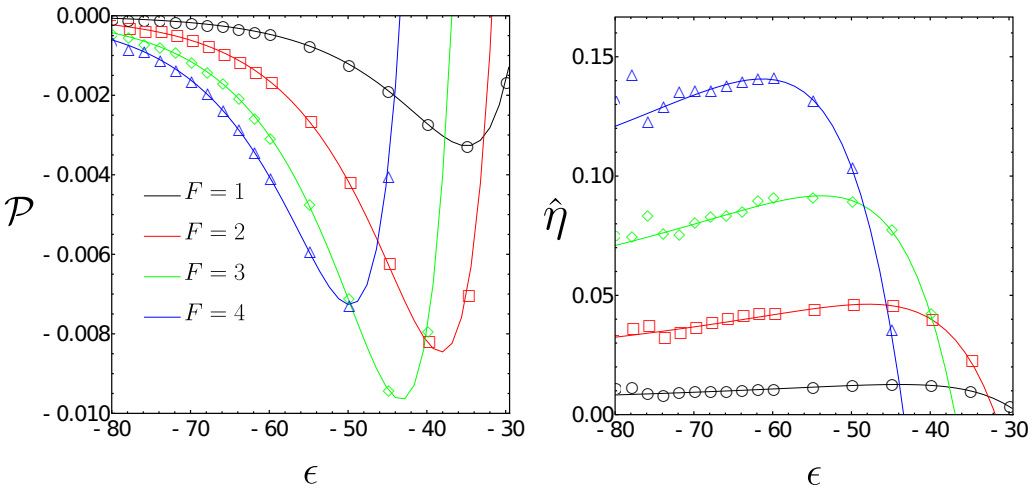

FIG. 11. Model A, $q = 3$. Left and right panels show the power per unit $\mathcal{P} = \langle \mathrm{P} \rangle / N$ and efficiency $\hat{\eta}$ for $N = 2$ for different values of F. Continuous lines are exact solutions obtained from the microscopic master equation, while symbols come from numerical simulations using the Gillespie algorithm. Parameters: $\alpha = 1$, $\beta_1 = 1$, and $\beta_2 = 0.4$.

driving depends on initial and final states and on the bath to which the system is coupled, i.e., $\mp F$ for the cold bath ($\nu = 1$) and $\pm F$ for the hot bath ($\nu = 2$). If N is finite, the dynamics can be simulated using a standard Gillespie algorithm [71].

In the thermodynamic limit $N \to \infty$, we can employ a mean-field approach. We introduce the mean occupation density of a given state, $p_{\uparrow(\downarrow)} = \langle \sum_i N^{(i)}_{\uparrow(\downarrow)} / N \rangle$, which are characterized only by the index of states, massively reducing the complexity of the equations. By employing the mean-field approximation of writing down any n-point correlations as the product of n averages, $p_{\uparrow(\downarrow)}$ is ruled by the master equation $\dot{p}_\beta = \sum_{\nu=1}^{2} J^{(\nu)}_{\beta\beta'}$, where $J^{(\nu)}_{\beta\beta'} = \omega^{(\nu)}_{\beta\beta'} p_{\beta'} - \omega^{(\nu)}_{\beta'\beta} p_\beta$ with transition rates listed below:

$$\omega^{(1)}_{\uparrow\downarrow} = \Gamma e^{-\frac{\beta_1}{2}\{-\epsilon(1+\alpha)(1-2p_\uparrow)-F\}} \quad \text{and}$$
$$\omega^{(2)}_{\uparrow\downarrow} = \Gamma e^{-\frac{\beta_2}{2}\{-\epsilon(1+\alpha)(1-2p_\uparrow)+F\}}, \tag{A2}$$

$$\omega^{(1)}_{\downarrow\uparrow} = \Gamma e^{-\frac{\beta_1}{2}\{\epsilon(1+\alpha)(1-2p_\uparrow)+F\}} \quad \text{and}$$
$$\omega^{(2)}_{\downarrow\uparrow} = \Gamma e^{-\frac{\beta_2}{2}\{\epsilon(1+\alpha)(1-2p_\uparrow)-F\}}. \tag{A3}$$

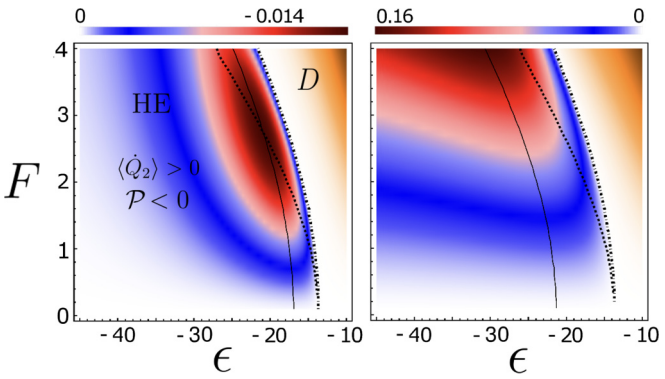

FIG. 12. Model A, $q = 3$ and $N = 2$. From left to right, top panels depict power per unit $\mathcal{P} = \langle \mathrm{P} \rangle / N$ and efficiency $\hat{\eta}$ heat maps. Heat engine and dud regimes are denoted by HE and D, respectively. For a better visualization, the pump regime has not been indicated. Parameters: $\alpha = 1$, $\beta_1 = 1$, and $\beta_2 = 0.4$.

Transition rates are evaluated in a similar fashion for $q = 3$. Starting with model A, they are identical to $q = 2$ for transitions of type $\uparrow \to \downarrow$ and $\downarrow \to \uparrow$, whereas the energy difference reads $\epsilon(N^{(i)}_k - \alpha N^{(i)}_\ell)/N$ for transitions like $0 \to \uparrow$ ($\downarrow$), where $k = \uparrow$ ($\downarrow$) and $\ell = \downarrow$ ($\uparrow$). All the remaining ones can be analogously computed. Likewise, for model B, a given transition $N^{(j)}_\ell = N^{(i)}_\ell - 1$ and $N^{(i)}_k = N^{(i)}_k + 1$ (where k, $\ell \in (\uparrow, 0, \downarrow)$) has energy difference given by $\epsilon(N^{(i)}_k - N^{(i)}_\ell + 1)/N$ [46,47]. Numerical simulations are performed as before, but now there are $2q(q-1) = 12$ distinct transitions. As for $q = 2$, the limit $N \to \infty$ is promptly obtained and described by the master equation $\dot{p}_\beta = \sum_{\nu=1}^{2} \sum_{\beta' \neq \beta} J^{(\nu)}_{\beta\beta'}$ [$\beta \in (\downarrow, 0, \uparrow)$]. For model A, some of the transition rates are

$$\omega^{(1)}_{\uparrow\downarrow} = \Gamma e^{-\frac{\beta_1}{2}\{-\epsilon(1+\alpha)(p_\downarrow - p_\uparrow)+F\}},$$
$$\omega^{(1)}_{\uparrow 0} = \Gamma e^{-\frac{\beta_1}{2}\{\epsilon(p_\uparrow - \alpha p_\downarrow)-F\}} \quad \text{and}$$
$$\omega^{(1)}_{0\downarrow} = \Gamma e^{-\frac{\beta_1}{2}\{\epsilon(\alpha p_\uparrow - p_\downarrow)-F\}}. \tag{A4}$$

For model B, we have

$$\omega^{(1)}_{\uparrow\downarrow} = \Gamma e^{-\frac{\beta_1}{2}\{\epsilon(p_\uparrow - p_\downarrow)+F\}},$$
$$\omega^{(1)}_{\uparrow 0} = \Gamma e^{-\frac{\beta_1}{2}\{\epsilon(p_\uparrow - p_0)-F\}} \quad \text{and}$$
$$\omega^{(1)}_{0\downarrow} = \Gamma e^{-\frac{\beta_1}{2}\{\epsilon(p_0 - p_\downarrow)-F\}} \tag{A5}$$

where all the others can be easily computed along the same line, remembering also that $\omega^{(2)}_{ij}$ is promptly obtained from $\omega^{(1)}_{ij}$ just by replacing $F \to -F$.

APPENDIX B: HEAT MAPS FOR Q = 3 AND N = 2 ENGINES

This section discusses two important aspects introduced in the main text: The reliability of numerical simulations for finite N and the fact that a minimal setup of $N = 2$ interacting units already captures the essential ingredients of the model. Results are shown for $\beta_1 = 1$ and $\beta_2 = 0.4$ only for the sake of a better visualization. Figure 11 compares thermodynamic

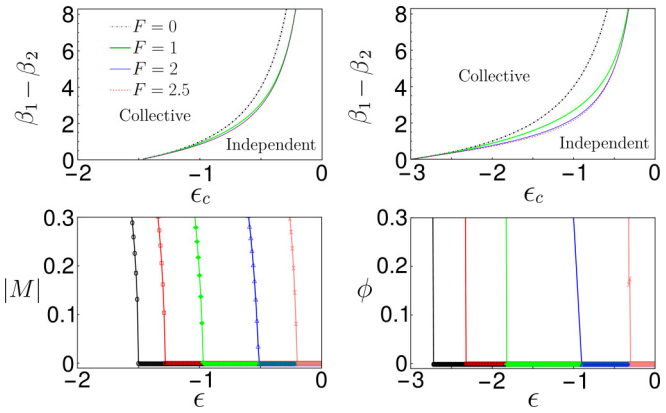

FIG. 13. For $q = 3$ and distinct F's, left and right top panels show the phase diagrams $\Delta\beta = \beta_1 - \beta_2$ vs ϵ_c for model A and B, respectively. They are obtained from the linear stability analysis of the disordered phase. For the sake of comparison, the bottom panels show (for $F = 1$) the location of phase transitions from the order-parameter behaviors. From left to right $\beta_1 - \beta_2 = 0, 1/3, 1, 3,$ and 9. In all cases, we set $\beta_2 = 1$.

quantities evaluated from numerical simulations (Gillespie algorithm) and those from exact steady probabilities computed from the microscopic master equation for $N = 2$. Figure 12 extends the heat maps to $N = 2$, showing that despite the substantial reduced performance, all characteristics from collective effects are already present in this minimal setup.

APPENDIX C: LINEAR STABILITY OF DISORDERED PHASE SOLUTION FOR MODELS A AND B FOR Q = 3

For completeness, we provide additional information about the crossover between collective and independent regimes for model A (when $\alpha = 1$) and B for $q = 3$, which manifests through continuous and discontinuous phase transitions, respectively. These phenomena can be analyzed in a similar way to their equilibrium counterparts, by means of two order parameters, M for model A and $\phi = (3p_{\max} - 1)/2$ ($p_{\max} = \max\{p_\downarrow^{st}, p_0^{st}, p_\uparrow^{st}\}$) for model B, with the first one characterized by the classical exponent $\beta = 1/2$ [77,78]. However, contrasting to the equilibrium Potts model, nonequilibrium ingredients modify the phase transition for model B from a continuous to a discontinuous one, as shown in Fig. 13(b).

A systematic investigation can be performed by means of a linear expansion of the master equation around a fixed point as follows $\dot{p}_m = \sum_n A_{mn} p_n$, where A is the Jacobian matrix with elements $A_{mn} = \partial(\omega_{mn}^{(1)} + \omega_{mn}^{(2)})/\partial p_n|_{p_n = p^*}$ evaluated at fixed points $\sum_n A_{mn} p_n^* = 0$. In particular, the solution p_n^* is linearly stable if the real parts of the eigenvalues of the Jacobian matrix are negative. In both cases, the independent regime is characterized by equal population $p_\downarrow^* = p_0^* = p_\uparrow^* = 1/3$ for $\epsilon \geqslant \epsilon_c$. In both cases introduced above, the corresponding eigenvalues can be written as $\lambda_\pm = \lambda_0 \pm \lambda_1$, with λ_0 given by

$$\lambda_0 = -(3 + \beta_1\epsilon)\cosh\left(\frac{\beta_1 F}{2}\right) - (3 + \beta_2\epsilon)\cosh\left(\frac{\beta_2 F}{2}\right), \tag{C1}$$

whereas λ_1, for model A, reads

$$\lambda_1 = \Bigg[6 + \epsilon^2(\beta_1^2 + \beta_2^2) + (\beta_1^2\epsilon^2 - 3)\cosh(\beta_1 F) - 3\cosh(\beta_2 F) + \beta_2\epsilon^2\Bigg(4\beta_1\cosh\left(\frac{\beta_1 F}{2}\right)\cosh\left(\frac{\beta_2 F}{2}\right) + \beta_2\cosh(\beta_2 F)\Bigg) + 12\sinh\left(\frac{\beta_1 F}{2}\right)\sinh\left(\frac{\beta_2 F}{2}\right)\Bigg]^{1/2}, \tag{C2}$$

while, for model B, we have

$$\lambda_1 = i\sqrt{3}\left[\sinh\left(\frac{\beta_1 F}{2}\right) - \sinh\left(\frac{\beta_2 F}{2}\right)\right]. \tag{C3}$$

Since λ_1 is imaginary for model B, the linear stability of disordered solution is granted provided $\lambda_0 < 0$. Conversely, for model A, due to the fact that β_1 and β_2 are always positive, λ_- is always negative. Conversely, λ_+ is always negative for sufficiently large and positive ϵ, with the order-disorder phase transition corresponding to a transcritical bifurcation when $\lambda_+ = 0$. Clearly, λ_+ becomes positive as ϵ decreases, meaning that the independent regimes turns unstable.

Figure 13 depicts the phase diagrams $\Delta\beta = \beta_1 - \beta_2$ versus ϵ for different F obtained from the linear analysis. In particular, for $F = 0$, λ_+'s and λ_-'s read -6 and $-2[3 + \epsilon(\beta_1 + \beta_2)]$ (model A) and $-[6 + \epsilon(\beta_1 + \beta_2)]$ (model B), respectively, consistent to phase transitions taking place at $\epsilon_c = -3/(\beta_1 + \beta_2)$ and $\epsilon_c = -6/(\beta_1 + \beta_2)$. The crossover from collective to independent regime smoothly changes with the driving and it is more sensitive to the difference of temperatures. Note the excellent agreement between the values of ϵ_c obtained from the linear analysis and those from order parameter behaviors (bottom panels for $F = 1$).

[1] S. Carnot, *Réflexions sur la puissance motrice du feu sur les machinés propre à développer cette puissance*, édition critique par Fox Robert, Vrin J, Paris (1978).

[2] F. Curzon and B. Ahlborn, Efficiency of a Carnot engine at maximum power output, Am. J. Phys. **43**, 22 (1975).

[3] U. Seifert, Stochastic thermodynamics, fluctuation theorems and molecular machines, Rep. Prog. Phys. **75**, 126001 (2012).

[4] G. Gallavotti and E. G. D. Cohen, Dynamical ensembles in nonequilibrium statistical mechanics, Phys. Rev. Lett. **74**, 2694 (1995).

[5] J. Kurchan, Fluctuation theorem for stochastic dynamics, J. Phys. A: Math. Gen. **31**, 3719 (1998).

[6] C. Jarzynski, Nonequilibrium equality for free energy differences, Phys. Rev. Lett. **78**, 2690 (1997).

[7] G. E. Crooks, Entropy production fluctuation theorem and the nonequilibrium work relation for free energy differences, Phys. Rev. E **60**, 2721 (1999).

[8] D. Collin Jr, F. Ritort, C. Jarzynski, S. B. Smith, I. Tinoco, and C. Bustamante, Verification of the crooks fluctuation theorem and recovery of RNA folding free energies, Nature (London) **437**, 231 (2005).

[9] T. P. Xiong, L. L. Yan, F. Zhou, K. Rehan, D. F. Liang, L. Chen, W. L. Yang, Z. H. Ma, M. Feng, and V. Vedral, Experimental verification of a Jarzynski-related information-theoretic equality by a single trapped ion, Phys. Rev. Lett. **120**, 010601 (2018).

[10] L.-L. Yan, J.-W. Zhang, M.-R. Yun, J.-C. Li, G.-Y. Ding, J.-F. Wei, J.-T. Bu, B. Wang, L. Chen, S.-L. Su, F. Zhou, Y. Jia, E.-J. Liang, and M. Feng, Experimental verification of dissipation-time uncertainty relation, Phys. Rev. Lett. **128**, 050603 (2022).

[11] G. Verley, M. Esposito, T. Willaert, and C. Van den Broeck, The unlikely Carnot efficiency, Nat. Commun. **5**, 4721 (2014).

[12] B. Cleuren, B. Rutten, and C. Van den Broeck, Universality of efficiency at maximum power, Eur. Phys. J.: Spec. Top. **224**, 879 (2015).

[13] C. Van den Broeck, Thermodynamic efficiency at maximum power, Phys. Rev. Lett. **95**, 190602 (2005).

[14] U. Seifert, Efficiency of autonomous soft nanomachines at maximum power, Phys. Rev. Lett. **106**, 020601 (2011).

[15] N. Golubeva and A. Imparato, Efficiency at maximum power of interacting molecular machines, Phys. Rev. Lett. **109**, 190602 (2012).

[16] K. Proesmans, B. Cleuren, and C. Van den Broeck, Power-efficiency-dissipation relations in linear thermodynamics, Phys. Rev. Lett. **116**, 220601 (2016).

[17] S. Ciliberto, Experiments in stochastic thermodynamics: Short history and perspectives, Phys. Rev. X **7**, 021051 (2017).

[18] M. V. S. Bonança, Approaching carnot efficiency at maximum power in linear response regime, J. Stat. Mech.: Theory Exp. (2019) 123203.

[19] M. Campisi and R. Fazio, The power of a critical heat engine, Nat. Commun. **7**, 11895 (2016).

[20] I. N. Mamede, P. E. Harunari, B. A. N. Akasaki, K. Proesmans, and C. E. Fiore, Obtaining efficient thermal engines from interacting Brownian particles under time-periodic drivings, Phys. Rev. E **105**, 024106 (2022).

[21] C. E. Fernandez Noa, A. L. L. Stable, W. G. C. Oropesa, A. Rosas, and C. E. Fiore, Efficient asymmetric collisional Brownian particle engines, Phys. Rev. Res. **3**, 043152 (2021).

[22] P. E. Harunari, F. S. Filho, C. E. Fiore, and A. Rosas, Maximal power for heat engines: Role of asymmetric interaction times, Phys. Rev. Res. **3**, 023194 (2021).

[23] D. Guéry-Odelin, A. Ruschhaupt, A. Kiely, E. Torrontegui, S. Martínez-Garaot, and J. G. Muga, Shortcuts to adiabaticity: Concepts, methods, and applications, Rev. Mod. Phys. **91**, 045001 (2019).

[24] S. Deffner and M. V. Bonança, Thermodynamic control—An old paradigm with new applications, Europhys. Lett. **131**, 20001 (2020).

[25] N. Pancotti, M. Scandi, M. T. Mitchison, and M. Perarnau-Llobet, Speed-ups to isothermality: Enhanced quantum thermal machines through control of the system-bath coupling, Phys. Rev. X **10**, 031015 (2020).

[26] X.-H. Zhao, Z.-N. Gong, and Z. C. Tu, Microscopic low-dissipation heat engine via shortcuts to adiabaticity and shortcuts to isothermality, Phys. Rev. E **106**, 064117 (2022).

[27] F. S. Gnesotto, F. Mura, J. Gladrow, and C. P. Broedersz, Broken detailed balance and non-equilibrium dynamics in living systems: A review, Rep. Prog. Phys. **81**, 066601 (2018).

[28] P. Smith and M. Schuster, Public goods and cheating in microbes, Curr. Biol. **29**, R442 (2019).

[29] C. W. Lynn, E. J. Cornblath, L. Papadopoulos, M. A. Bertolero, and D. S. Bassett, Broken detailed balance and entropy production in the human brain, Proc. Natl. Acad. Sci. USA **118**, e2109889118 (2021).

[30] R. Rao and M. Esposito, Nonequilibrium thermodynamics of chemical reaction networks: Wisdom from stochastic thermodynamics, Phys. Rev. X **6**, 041064 (2016).

[31] D. M. Busiello, S. Liang, F. Piazza, and P. De Los Rios, Dissipation-driven selection of states in non-equilibrium chemical networks, Commun. Chem. **4**, 16 (2021).

[32] A. V. Dass, T. Georgelin, F. Westall, F. Foucher, P. De Los Rios, D. M. Busiello, S. Liang, and F. Piazza, Equilibrium and non-equilibrium furanose selection in the ribose isomerisation network, Nat. Commun. **12**, 2749 (2021).

[33] S. Liang, D. M. Busiello, and P. De Los Rios, Emergent thermophoretic behavior in chemical reaction systems, New J. Phys. **24**, 123006 (2022).

[34] P. Bonifazi, M. Goldin, M. A. Picardo, I. Jorquera, A. Cattani, G. Bianconi, A. Represa, Y. Ben-Ari, and R. Cossart, Gabaergic hub neurons orchestrate synchrony in developing hippocampal networks, Science **326**, 1419 (2009).

[35] E. Schneidman, M. J. Berry, R. Segev, and W. Bialek, Weak pairwise correlations imply strongly correlated network states in a neural population, Nature (London) **440**, 1007 (2006).

[36] G. Buzsáki and K. Mizuseki, The log-dynamic brain: How skewed distributions affect network operations, Nat. Rev. Neurosci. **15**, 264 (2014).

[37] E. Gal, M. London, A. Globerson, S. Ramaswamy, M. W. Reimann, E. Muller, H. Markram, and I. Segev, Rich cell-type-specific network topology in neocortical microcircuitry, Nat. Neurosci. **20**, 1004 (2017).

[38] R. Tönjes, C. E. Fiore, and T. Pereira, Coherence resonance in influencer networks, Nat. Commun. **12**, 72 (2021).

[39] V. Mukherjee and U. Divakaran, Many-body quantum thermal machines, J. Phys.: Condens. Matter **33**, 454001 (2021).

[40] W. Niedenzu and G. Kurizki, Cooperative many-body enhancement of quantum thermal machine power, New J. Phys. **20**, 113038 (2018).

[41] D. Kolisnyk and G. Schaller, Performance boost of a collective qutrit refrigerator, Phys. Rev. Appl. **19**, 034023 (2023).

[42] C. L. Latune, I. Sinayskiy, F. Petruccione, Collective heat capacity for quantum thermometry and quantum engine enhancements, New J. Phys. **22**, 083049 (2020).

[43] S. Kamimura, H. Hakoshima, Y. Matsuzaki, K. Yoshida, and Y. Tokura, Quantum-enhanced heat engine based on superabsorption, Phys. Rev. Lett. **128**, 180602 (2022).

[44] M. A. Macovei, Performance of the collective three-level quantum thermal engine, Phys. Rev. A **105**, 043708 (2022).

[45] H. Vroylandt, M. Esposito, and G. Verley, Collective effects enhancing power and efficiency, Europhys. Lett. **120**, 30009 (2017).

[46] T. Herpich, J. Thingna, and M. Esposito, Collective power: Minimal model for thermodynamics of nonequilibrium phase transitions, Phys. Rev. X **8**, 031056 (2018).

[47] T. Herpich and M. Esposito, Universality in driven Potts models, Phys. Rev. E **99**, 022135 (2019).

[48] M. Suñé and A. Imparato, Out-of-equilibrium clock model at the verge of criticality, Phys. Rev. Lett. **123**, 070601 (2019).

[49] J. T. Young, A. V. Gorshkov, M. Foss-Feig, and M. F. Maghrebi, Nonequilibrium fixed points of coupled Ising models, Phys. Rev. X **10**, 011039 (2020).
[50] J. M. Yeomans, *Statistical Mechanics of Phase Transitions* (Clarendon Press, Oxford, 1992).
[51] F. Y. Wu, The Potts model, Rev. Mod. Phys. **54**, 235 (1982).
[52] M. Blume, V. J. Emery, and R. B. Griffiths, Ising model for the λ transition and phase separation in He^3-He^4 mixtures, Phys. Rev. A **4**, 1071 (1971).
[53] W. Hoston and A. N. Berker, Multicritical phase diagrams of the Blume-Emery-Griffiths model with repulsive biquadratic coupling, Phys. Rev. Lett. **67**, 1027 (1991).
[54] D. M. Busiello, D. Gupta, and A. Maritan, Coarse-grained entropy production with multiple reservoirs: Unraveling the role of time scales and detailed balance in biology-inspired systems, Phys. Rev. Res. **2**, 043257 (2020).
[55] M. Esposito, Stochastic thermodynamics under coarse graining, Phys. Rev. E **85**, 041125 (2012).
[56] D. M. Busiello, J. Hidalgo, and A. Maritan, Entropy production for coarse-grained dynamics, New J. Phys. **21**, 073004 (2019).
[57] D. M. Busiello and A. Maritan, Entropy production in master equations and Fokker–Planck equations: Facing the coarse-graining and recovering the information loss, J. Stat. Mech.: Theory Exp. (2019) 104013.
[58] S. R. Salinas, Introduction to statistical methods, in *Introduction to Statistical Physics* (Springer, New York, 2001), pp. 1–17.
[59] S. Liepelt and R. Lipowsky, Kinesin's network of chemomechanical motor cycles, Phys. Rev. Lett. **98**, 258102 (2007).
[60] S. Liepelt and R. Lipowsky, Operation modes of the molecular motor kinesin, Phys. Rev. E **79**, 011917 (2009).
[61] C. Berton, D. M. Busiello, S. Zamuner, E. Solari, R. Scopelliti, F. Fadaei-Tirani, K. Severin, and C. Pezzato, Thermodynamics and kinetics of protonated merocyanine photoacids in water, Chem. Sci. **11**, 8457 (2020).
[62] C. Berton, D. M. Busiello, S. Zamuner, R. Scopelliti, F. Fadaei-Tirani, K. Severin, and C. Pezzato, Light-switchable buffers, Angew. Chem., Int. Ed. **60**, 21737 (2021).
[63] P. De Los Rios and A. Barducci, Hsp70 chaperones are non-equilibrium machines that achieve ultra-affinity by energy consumption, eLife **3**, e02218 (2014).
[64] P. Goloubinoff and P. De Los Rios, The mechanism of Hsp70 chaperones:(entropic) pulling the models together, Trends Biochem. Sci. **32**, 372 (2007).
[65] J. Schnakenberg, Network theory of microscopic and macroscopic behavior of master equation systems, Rev. Mod. Phys. **48**, 571 (1976).
[66] H. B. Callen, *Thermodynamics and an Introduction to Thermostatistics* (Wiley, New York, 1998).
[67] K. Proesmans and C. Van den Broeck, Onsager coefficients in periodically driven systems, Phys. Rev. Lett. **115**, 090601 (2015).
[68] K. Proesmans, Y. Dreher, M. C. V. Gavrilov, J. Bechhoefer, and C. Van den Broeck, Brownian duet: A novel tale of thermodynamic efficiency, Phys. Rev. X **6**, 041010 (2016).
[69] K. Proesmans and C. E. Fiore, General linear thermodynamics for periodically driven systems with multiple reservoirs, Phys. Rev. E **100**, 022141 (2019).
[70] O. Kedem and S. R. Caplan, Degree of coupling and its relation to efficiency of energy conversion, Trans. Faraday Soc. **61**, 1897 (1965).
[71] D. T. Gillespie, Exact stochastic simulation of coupled chemical reactions, J. Phys. Chem. **81**, 2340 (1977).
[72] F. Jülicher and J. Prost, Cooperative molecular motors, Phys. Rev. Lett. **75**, 2618 (1995).
[73] Y. Tu, The nonequilibrium mechanism for ultrasensitivity in a biological switch: Sensing by Maxwell's demons, Proc. Natl. Acad. Sci. USA **105**, 11737 (2008).
[74] J. M. Horowitz and M. Esposito, Thermodynamics with continuous information flow, Phys. Rev. X **4**, 031015 (2014).
[75] G. Nicoletti and D. M. Busiello, Mutual information disentangles interactions from changing environments, Phys. Rev. Lett. **127**, 228301 (2021).
[76] G. Tkačik and W. Bialek, Information processing in living systems, Annu. Rev. Condens. Matter Phys. **7**, 89 (2016).
[77] C. E. Fiore and M. G. E. da Luz, Exploiting a semi-analytic approach to study first order phase transitions, J. Chem. Phys. **138**, 014105 (2013).
[78] M. S. S. Challa, D. P. Landau, and K. Binder, Finite-size effects at temperature-driven first-order transitions, Phys. Rev. B **34**, 1841 (1986).